

## Article

# Improve the Performance of SONOS Type UV TD Sensors Using IOHAOS with Enhanced UV Transparency ITO Gate

Wen-Ching Hsieh <sup>1,\*</sup>, Fun-Cheng Jong <sup>2</sup> and Wei-Ting Tseng <sup>1</sup>

<sup>1</sup> Opto-Electronic System Engineering Department, Minghsin University of Science and Technology, Xinfeng 30401, Taiwan; saes91014300@gmail.com

<sup>2</sup> Electronic Engineering Department, Southern Taiwan University of Science and Technology, Nan-Tai Street, Yungkuang District, Tainan 71005, Taiwan; fcjong@mail.stust.edu.tw

\* Correspondence: wchsieh@must.edu.tw

**Abstract:** This research demonstrates that an indium tin oxide–silicon oxide–hafnium aluminum oxide–silicon oxide–silicon device with enhanced UV transparency ITO gate (hereafter E-IOHAOS) can greatly increase the sensing response performance of a SONOS type ultraviolet radiation total dose (hereafter UV TD) sensor. Post annealing process is used to optimize UV optical transmission and electrical resistivity characterization in ITO film. Via nano-columns (NCol)s crystalline transformation of ITO film, UV transparency of ITO film can be enhanced. UV radiation causes the threshold voltage  $V_T$  of the E-IOHAOS device to increase, and the increase of the  $V_T$  of E-IOHAOS device is also related to the UV TD. The experimental results show that under UV TD irradiation of  $100 \text{ mW}\cdot\text{s}/\text{cm}^2$ , ultraviolet light can change the threshold voltage  $V_T$  of E-IOHAOS to 12.5 V. Moreover, the  $V_T$  fading rate of ten-years retention on E-IOHAOS is below 10%. The  $V_T$  change of E-IOHAOS is almost 1.25 times that of poly silicon–aluminum oxide–hafnium aluminum oxide–silicon oxide–silicon with poly silicon gate device (hereafter SAHAOS). The sensing response performance of an E-IOHAOS UV TD sensor is greatly improved by annealed ITO gate.

**Keywords:** nano column; IOHAOS; UV; TD; sensor



**Citation:** Hsieh, W.-C.; Jong, F.-C.; Tseng, W.-T. Improve the Performance of SONOS Type UV TD Sensors Using IOHAOS with Enhanced UV Transparency ITO Gate. *Coatings* **2021**, *11*, 408. <https://doi.org/10.3390/coatings11040408>

Academic Editor: You Seung Rim

Received: 4 February 2021

Accepted: 29 March 2021

Published: 1 April 2021

**Publisher's Note:** MDPI stays neutral with regard to jurisdictional claims in published maps and institutional affiliations.



**Copyright:** © 2021 by the authors. Licensee MDPI, Basel, Switzerland. This article is an open access article distributed under the terms and conditions of the Creative Commons Attribution (CC BY) license (<https://creativecommons.org/licenses/by/4.0/>).

## 1. Introduction

Ultraviolet (UV) is widely used in a variety of applications such as safety, medicine, defense, and industry [1,2]. Ultraviolet light (UV) is a form of electromagnetic radiation, which can be classified into three types according to its wavelength. Ultraviolet C (UVC) with wavelengths between 100 and 280 nm is totally absorbed by the stratospheric ozone layer (O<sub>3</sub>). Ultraviolet B (UVB) with wavelengths between 280 and 315 nm is partially absorbed by the stratospheric ozone layer (O<sub>3</sub>). Ultraviolet A (UVA) with wavelengths between 315 and 400 nm is slightly absorbed by the atmosphere [1,2]. The ultraviolet radiation can cause eye damage, skin damage, DNA damage, and other health damage. It is important to monitor the total dose of ultraviolet radiation (UV TD). Recently, many studies have been performed to measure the ultraviolet radiation in various environments [1,2].

### 1.1. UV TD Sensing Techniques in Semiconductor Technology

#### 1.1.1. Conventional Semiconductor Sensors for UV

There are three kinds of conventional semiconductor sensors for UV radiation:

1. PIN diode type sensor;
2. Item MOS type sensor;
3. Thermal luminescent dosimeters (TLDs) type sensor [3–5].

In the case of a PIN diode type sensor, a higher bias is applied and a smaller current is measured. Therefore, the diode should have larger size to increase the sensitivity of the PIN photo diode type sensor.

For the metal oxide MOS type sensor, the charge generated by radiation is unstable. When the sensor data is read, the charge generated by the radiation will be released.

For the TLD sensor, the UV TD data is obtained by measuring the thermal luminescence of the TLD after UV exposure. However, the system for reading of thermal luminescence is complex.

The three sensors have some disadvantages: such as high cost, large size, and complex reading system [6–10]. This is important for shrinking semiconductor sensors in advanced nano-semiconductor processes. In addition, both of PIN and MOS sensors are radiation intensity sensors, not radiation TD sensors. The data reading of PIN and MOS sensors will be volatile and is independent of the radiation TD [6–10].

#### 1.1.2. SONOS NVM Type UV TD Sensor

The disadvantages of three conventional UV sensors can be resolved by using non-volatile memory (NVM) semiconductor devices as UV TD sensors. Floating gate storage (FG) devices have limitations in reducing device size and simplifying manufacturing processes. Therefore, the gate length of silicon-silicon oxide-silicon nitride-silicon oxide-silicon (SONOS) NVM device has been shown to be reduced to the nanoscale. Moreover, the SONOS NVM has the superiority of coupling-free and MOS-like structure. The SONOS structure type device is a hopeful next-generation NVM device. In previous studies, a SONOS-like NVM device has been proven to be potentially used as non-volatile UV TD sensors [11,12]. UV generated charges can be captured inside the trapping layer of the SONOS NVM device permanently. The change of the amount of trapped charge inside the SONOS NVM trapping layer can be detected by an external circuit after UV exposure. The SONOS-type NVM UV TD sensor has many advantages compared with a conventional UV sensor [11,12]:

1. Size is small;
2. Output data is dependent on UV TD;
3. Output data is nonvolatile;
4. Output data can be erased;
5. Using high-k semiconductor technology;
6. Data reading equipment is simple;
7. Sensitivity is tunable.

Since the feature size of the next generation MOS should be reduced, MOS devices should face the challenge of reducing the gate length and gate dielectric layer thickness. As a result, the high k material was used as a gate dielectric in the next generation of MOS devices. In next generation, a silicon-silicon dioxide-hafnium oxide-silicon dioxide-silicon (SOHOS) like device with high-k gate dielectric materials have better performance of NVM than silicon-silicon oxide-silicon nitride-silicon oxide-silicon SONOS due to their scalability [13–17]. In former studies, a poly silicon-aluminum oxide-hafnium aluminum oxide-silicon oxide-silicon SAHAOS with poly silicon gate device has shown the better performance as NVM UV TD sensor than a silicon-silicon oxide-silicon nitride-silicon oxide-silicon SONOS sensor [18–20].

This research demonstrates that an indium tin oxide-silicon oxide-hafnium aluminum oxide-silicon oxide-silicon device with enhanced UV transparency ITO gate (hereafter E-IOHAOS) can greatly increase the sensing response of a SONOS type ultraviolet radiation total dose (hereafter UV TD) sensor. The post annealing process is used to optimize UV optical transmission and electrical resistivity characterization in ITO film. Via nanocolumns (NCols) crystalline transformation, UV transparency of ITO film can be enhanced by the temperature annealing process [21–24]. This study shows that an E-IOHAOS with NCols crystalline ITO can greatly improve the sensing response of a nonvolatile UV TD sensor. UV radiation causes the threshold voltage  $V_T$  of the E-IOHAOS device to increase, and the increase of the  $V_T$  of E-IOHAOS device is also related to the UV TD. Moreover, the  $V_T$  fading rate of ten-years retention on E-IOHAOS is also good. The UV-induced  $V_T$  shift of E-IOHAOS is significantly better than that of poly silicon-aluminum oxide-hafnium

aluminum oxide–silicon oxide–silicon with poly silicon gate SAHAOS. In this paper, the performance of indium tin oxide–silicon oxide–hafnium aluminum oxide–silicon oxide–silicon (hereafter IOHAOS) with different crystal structure ITO is compared. From this study, it was found that E-IOHAOS devices with NCol crystal ITO could significantly improve the response of SONOS-type UV TD sensors. The  $V_T$  shift of E-IOHAOS is almost 1.25 times that of poly silicon–aluminum oxide–hafnium aluminum oxide–silicon oxide–silicon SAHAOS with poly silicon gate device. The sensing response of an E-IOHAOS UV TD sensor is greatly improved by the annealed ITO gate. These results strongly suggest that E-IOHAOS could be the most promising candidate for next-generation nonvolatile UV TD sensor technology.

### 1.2. ITO Photo Electric Characterizations for the UV TD Sensor

Tin oxide (ITO) is widely used as a transparent anode. Due to ITO having many good characteristics, such as good conductivity, good mechanical strength, good optical transmission, good chemical stability, and wide bandwidth (ranging from 3.5 to 4.2 eV), ITO materials are widely used as contact electrodes for many optoelectronic devices, such as flat panel displays, solar cells, LED, and other fields. ITO film can be deposited using several methods, including spin-coating, electron beam evaporation, advanced pulsed laser deposition, metal organic chemical vapor deposition, and RF magnetron sputtering [25–30]. ITO has good photoelectric characterizations including electrical conductivity and good optical transparency in the visible range. However, when the ITO film is used as the UV transparent conductive oxide TCO of the UV transparent photoelectric device, the optical transparency in the UV range should be improved. The post annealing process is used to optimize UV optical transmission and electrical resistivity characterization in ITO film. Via nanocolumns (NCol) crystalline transformation of ITO film, UV transparency of ITO film can be enhanced [21–24]. This study shows that the UV optical transmittance and electrical conductivity of ITO film can be improved by the post annealing process.

### 1.3. SONOS NVM Type UV TD Sensor Operation Mechanisms

The reaction of UV TD to the SONOS NVM type UV TD sensor can be described as five reactions [11,12].

#### 1.3.1. Data Writing

1. The electron-hole pairs are generated by UV radiation in the substrate of the SONOS NVM type UV TD sensor.
2. The UV generated electron-hole pairs in the substrate are separated by positive gate voltage (hereafter PGV).
3. Then, through PGV, these negative charges are swept over the  $\text{SiO}_2$  tunneling layer of the SONOS NVM type UV TD and are injected into the trapping layer of the SONOS NVM type UV TD sensor.
4. Then, some of these negative charges are captured by the trapping layer of the SONOS NVM UV TD sensor, and then the captured charge accumulates permanently in the capture layer of the SONOS NVM UV TD sensor.

#### 1.3.2. Data Read

Data read: The amount of UV caused charge accumulated in the capture layer of the SONOS NVM UV TD sensor depends on the UV TD. We used the HP4284  $C_G$ - $V_G$  meter to measure changes in the  $C_G$ - $V_G$  curve after UV TD exposure.

#### 1.3.3. Data Erase

Data erase: By injecting positive charges under negative gate bias stress (hereafter referred to as NGV), the UV TD data in the SONOS-like NVM UV TD sensor device can be erased to the original invalid preirradiated state.

## 2. Experimental Section

### 2.1. Six Layer Structure Sensor Device

The SONOS NVM type UV TD sensor devices had six-layer structures in this study: Numbered lists can be added as follows:

1. Substrate: p-type Si <100> substrate (15–25 ohm-cm);
2. Charge tunneling layer: silicon oxide SiO<sub>2</sub> (3–7 nm);
3. Charge storage layer: hafnium aluminum oxide HfAlO (50–100 nm);
4. Charge blocking layer: silicon oxide SiO<sub>2</sub> (10–20 nm);
5. Gate electrode: indium tin oxide ITO (200–400 nm);
6. Substrate back side ohmic contact: Aluminum Al (200–400 nm).

In Figure 1, the cross-sectional view of SONOS type IOHAOS UV TD sensor is shown.

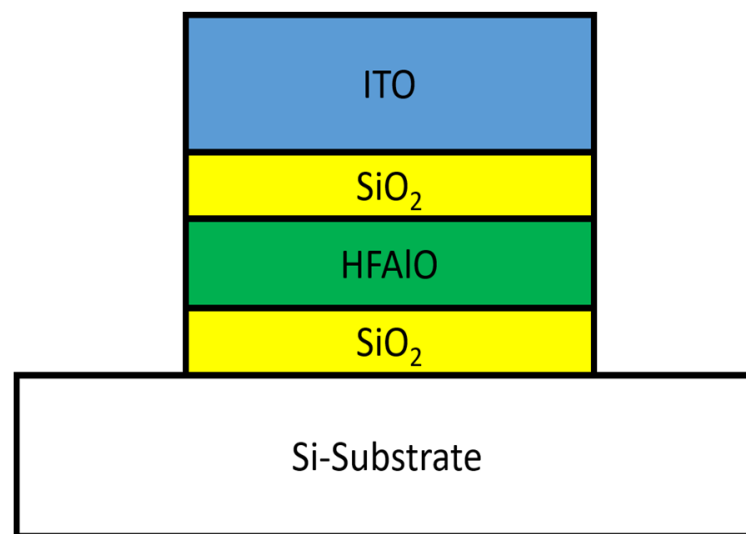


**Figure 1.** Cross-sectional view of the IOHAOS capacitor device.

### 2.2. Sensor Manufacture Detail

Eight manufacture steps for the IOHAOS UV TD sensor were used in the study:

1. Substrate: we used p-type Si <100> substrate with a resistivity of 15–25 ohm-cm as the substrate;
2. Tunneling oxide: we used silicon oxide SiO<sub>2</sub> as tunneling oxide thermally grown by an advanced clustered vertical furnace (ASM A-400) at 925 °C;
3. Trapping oxide: we used hafnium aluminum oxide HfAlO films with 10–40% Al as composition ratio as trapping oxide deposited by a metal organic chemical vapor deposition MOCVD system (AIXTRON Tricent 800016) at 400–550 °C;
4. Blocking oxide: we used SiO<sub>2</sub> as blocking oxide by low-pressure chemical vapor deposited by LPCVDD (SVCS Furnace system);
5. PDA: we processed post dielectric annealing (PDA) at different temperatures by a rapid thermal annealing (RTA) (KORONA RTP 800) machine in N<sub>2</sub> ambient;
6. Gate electrode: we used the indium tin oxide ITO (200–400 nm) as gate electrode deposited by a sputter machine (Fulintec-FSE). ITO ceramics target with 90% (wt. ratio) In<sub>2</sub>O<sub>3</sub> and 10% (wt. ratio) SnO<sub>2</sub> was used;
7. PMA: we processed post gate conductor annealing (PMA) at different temperatures by a rapid thermal annealing (RTA) process in N<sub>2</sub> ambient;
8. Substrate back side ohmic contact: we used aluminum Al sputtered by the sputter machine. (Duratek) In Figure 2, the manufacture process flow of the nonvolatile IOHAOS UV TD sensor is shown.

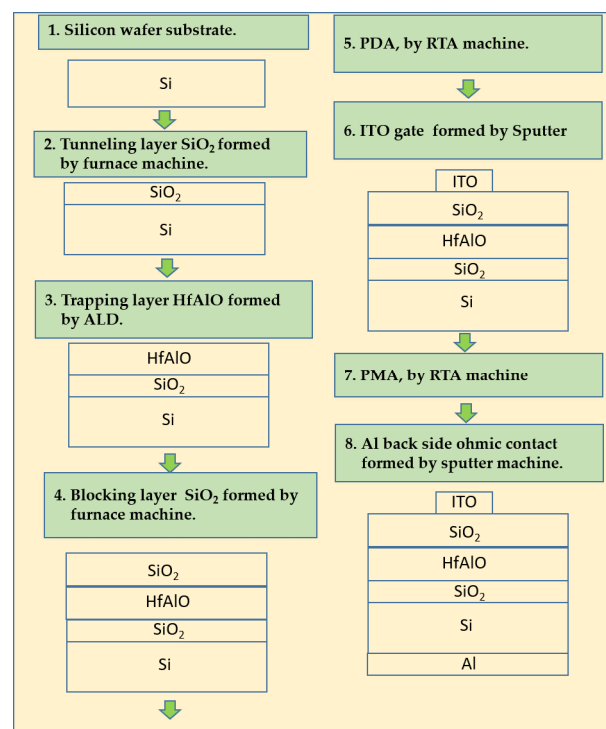


**Figure 2.** IOHAOS sensor fabrication flow.

To compare the UV TD SONOS type sensor performance for IOHAOS devices with different PDA and PMA temperatures, six types of IOHAOS with different PDA and PMA temperatures were fabricated, as shown in Table 1. To compare the UV TD SONOS type sensor performance for IOHAOS devices with different PMA temperatures, three types of IOHAOS with different PMA temperatures were fabricated:

**Table 1.** IOHAOS devices prepared with various anneal processes.

Split	I2H1	I2H2	I2H3	I1H2	I2H2	I3H2
Gate conductor layer anneal PMA temperature (°C)	500	500	500	250	500	600
Gate conductor layer anneal PMA time	30 s					
Gate conductor layer material	ITO	ITO	ITO	ITO	ITO	ITO
Gate dielectric layer anneal PDA temperature (°C)	900	1000	1100	1000	1000	1000
Gate dielectric layer anneal PDA time	30 s					
Gate dielectric layer material	HfAlO	HfAlO	HfAlO	HfAlO	HfAlO	HfAlO

1. IOHAOS with 250 °C 30 s PMA (hereafter IOHAOS-I1);
2. IOHAOS with 500 °C 30 s PMA (hereafter IOHAOS-I2);
3. IOHAOS with 600 °C 30 s PMA (hereafter IOHAOS-I3).

To compare the UV TD SONOS type sensor performance for IOHAOS devices with different PDA temperatures, three types of IOHAOS with different PDA temperatures were fabricated:

1. IOHAOS with 900 °C 30 s PDA (hereafter IOHAOS-H1);
2. IOHAOS with 1000 °C 30 s PDA (hereafter IOHAOS-H2);
3. IOHAOS with 1100 °C 30 s PDA (hereafter IOHAOS-H3).

In this study, these IOHAOS capacitor devices with different PDA and PMA had the same thickness of the tunneling oxide, trapping oxide, blocking oxide layer, and control gate layer for the IOHAOS UV TD sensor performance comparison. The various IOHAOS devices prepared with various PMA and PDA are listed in Table 1.

### 2.3. UV TD Sensor Operation Measurement

Three procedures for the SONOS-like NVM UV TD sensor operation in this study:

1. Data erase: By injecting positive charges under negative gate bias stress (hereafter referred to as NGV), the UV TD data in the SONOS-like NVM UV TD sensor device can be erased to the original invalid preirradiated state;
2. Data write: Both UV and positive gate bias (PGV) were applied to the SONOS-like NVM UV TD sensor device in the process of the writing of UV TD information. Both 405 nm and 375 nm wavelength was used for the UV radiation source.
3. Data read: The change of the amount of trapped charge inside the SONOS NVM trapping layer can be detected by an external circuit after UV exposure. We used the HP4284  $C_G$ - $V_G$  meter to measure changes in the  $C_G$ - $V_G$  curve after UV TD exposure.

In Figure 3, the SONOS-like NVM UV TD sensor device operation process flow of the nonvolatile SONOS-like NVM UV TD sensor device is shown. Various UV TD, PGV, and UV wavelength conditions for SONOS-like NVM UV TD sensor device are listed in Table 2.

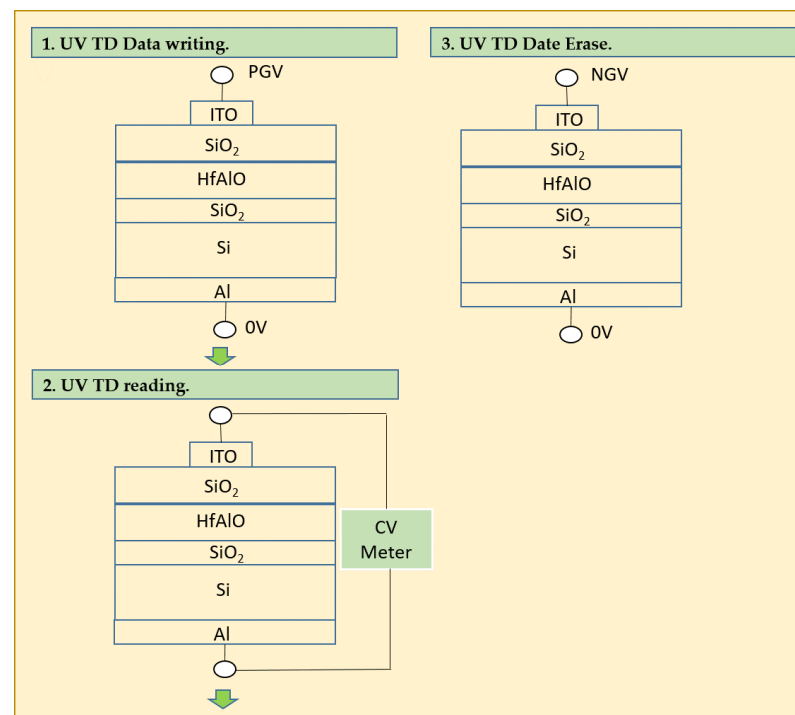


**Figure 3.** IOHAOS total does of ultraviolet radiation (UV TD) sensor operation flow.

**Table 2.** Symbol list of various UV TD, positive gate voltage (PGV), and UV wavelength conditions on IOHAOS.

Symbol	UV TD (mW·s/cm <sup>2</sup> )	PGV (V)	UV Wavelength (nm)
405U0G0	0 mW·s/cm <sup>2</sup>	0 V	405
405U100G5	100 mW·s/cm <sup>2</sup>	5 V	405
405U100G10	100 mW·s/cm <sup>2</sup>	10 V	405
405U100G20	100 mW·s/cm <sup>2</sup>	20 V	405
405U100G25	100 mW·s/cm <sup>2</sup>	25 V	405
375U100G25	100 mW·s/cm <sup>2</sup>	25 V	375

#### 2.4. Sensor Material Analysis

There are three methods for sensor material inspection in this study:

1. TEM: transmission electron microscopy (TEM) (JEM-2010F, JEOL USA Ltd, Peabody, MA., USA) was used for the crystallization analysis of the various IOHAOS with various PDA and PMA temperature conditions;
2. XRD: X-ray diffraction analysis (XRD) (Malvern Panalytical's X'Pert, Malvern Panalytical Ltd, Malvern, United Kingdom) was used for crystallization analysis of the various IOHAOS with various PMA temperature conditions;
3. Optical spectrometer: optical transmission spectroscopy analysis machine (Shimadzu UV-250, Shimadzu Corporation, Kyoto, Japan) was used for optical transmission analysis of various ITO control gate films material prepared with various post anneal temperature conditions.

#### 2.5. ITO Thin Film Prepare for Optical Transmission Measurement

To compare the optical transmission of ITO thin film with different anneal temperatures, three types of ITO thin film on glass substrate with different anneal temperatures were prepared, as shown in Table 3. Glass substrate was used to measure the optical transmittance of the ITO thin films. The three types of ITO thin film with different anneal temperatures are listed in Table 3. The thickness of these three ITO thin films on the glass substrate is the same as that of the control gate of three IOHAOS sensors devices. Three types of ITO were:

**Table 3.** ITO thin film on glass prepared with various anneal processes.

Split	I1	I2	I3
ITO thin film anneal temperature (°C)	250	500	600
ITO thin film anneal time	30 s	30 s	30 s

1. I1: ITO thin film (200~400 nm) on glass with 250 °C 30 s anneal temperatures (hereafter I1);
2. I2: ITO thin film (200~400 nm) on glass with 500 °C 30 s anneal temperatures (hereafter I2);
3. I3: ITO thin film (200~400 nm) on glass with 600 °C 30 s anneal temperatures (hereafter I3).

### 3. Results

#### 3.1. UV-Induced $V_T$ Shift in IOHAOS

Figure 4a displays a  $C_G$ - $V_G$  curve for an IOHAOS-I2H2 capacitor device with 500 °C 30 s ITO PMA and 1000 °C 30 s HfAlO PDA before UV irradiation. Figure 4b displays a  $C_G$ - $V_G$  curve for an IOHAOS-I2H2 capacitor device after 100 mW·s/cm<sup>2</sup> UV irradiation under PGV 25 V. The  $C_G$ - $V_G$  curve of the IOHAOS-I2H2 capacitor changed to the right after UV TD up to 100 mW·s/cm<sup>2</sup> at PGV 25 V, as displayed in Figure 4b. The UV-induced threshold voltage  $V_T$  change of IOHAOS-I2H2 was nearly 12.5 V under 405U100G25 UV irradiation, as displayed in Figure 4. This positive  $V_T$  shift result is the same as former research [11,12]. The sensing performance of IOHAOS-I2H2 was obtained from the experimental results; the sensitivity was greater than 10 KV·cm<sup>2</sup>/J, the resolution was less than 10 nJ/cm<sup>2</sup>, sensing range was about 10 nJ/cm<sup>2</sup> to 1 J/cm<sup>2</sup> for IOHAOS-I2H2 under 405G25 UV irradiation.

Figure 5 displays the relationship between the increase of  $V_T$  and UV TD for IOHAOS-I2H2 capacitors at 25 V PGV. Consistent with former studies, the increase in  $V_T$  in IOHAOS-I2H2 is concerning the increase in UV TD [11,12].

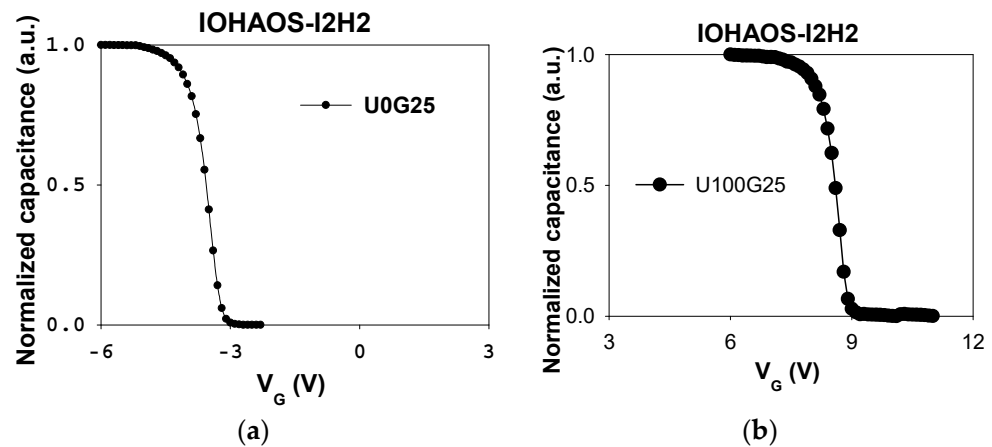


Figure 4.  $C_G$ - $V_G$  curve for an IOHAOS-I2H2 device (a) before UV irradiation and (b) after  $100 \text{ mW}\cdot\text{s}/\text{cm}^2$  UV TD irradiation at PGV 25 V.

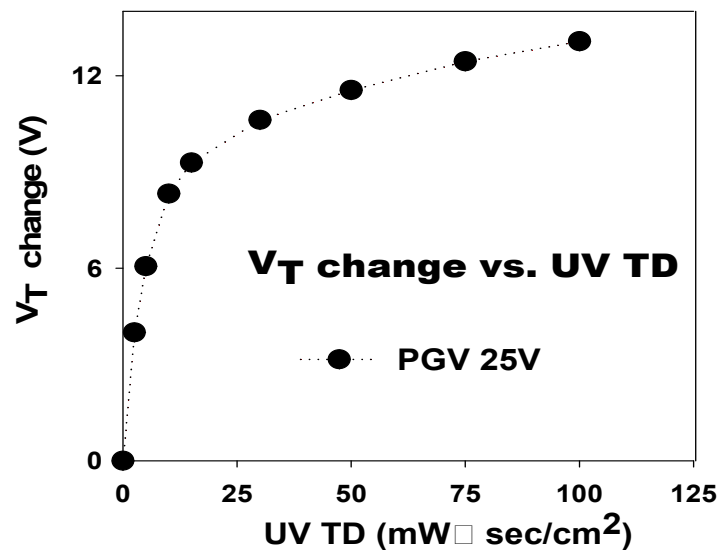
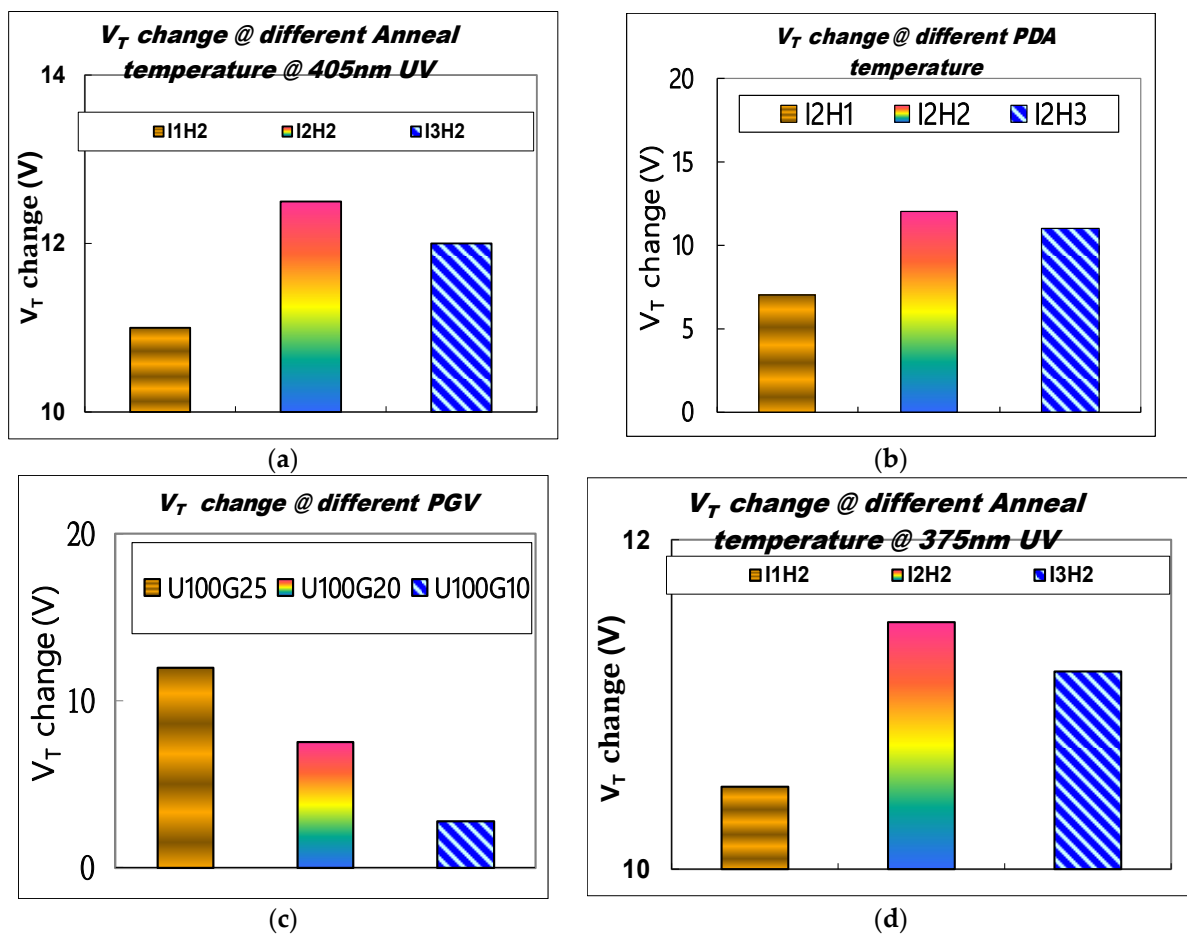


Figure 5. The dependence of the UV generated  $V_T$  increase on UV TD for an IOHAOS-I2H2 sensor under PGV 25 V.

### 3.2. UV-Induced $V_T$ Change Comparison for Various IOHAOS at Different Annealing Temperatures

Figure 6a shows the UV generated  $V_T$  change comparison for various IOHAOS capacitor devices with different ITO PMA temperatures after 405U100G25 irradiation condition. It is observed that the  $V_T$  change of IOHAOS-I2H2 (with  $500^\circ\text{C}$  30 s ITO PMA) was the most significant compared with IOHAOS-I1H2 and IOHAOS-I3H2 (with  $250^\circ\text{C}$  30 s and  $600^\circ\text{C}$  30 s ITO PMA) under 405U100G25 irradiation condition, as shown in Figure 6a. It is worth noting that, under the 405U100G25 irradiation condition, the  $V_T$  change of IOHAOS-I2H2 with  $500^\circ\text{C}$  30 s ITO PMA was almost 1.2 times greater than that of IOHAOS-I1H2 with  $250^\circ\text{C}$  30 s ITO PMA, as shown in Figure 6a. Figure 6d shows the UV generated  $V_T$  change comparison for various IOHAOS capacitor devices with different ITO PMA temperatures after 375U100G25 irradiation condition. It is observed that under 375U100G25 irradiation condition, the  $V_T$  change of IOHAOS-I2H2 with  $500^\circ\text{C}$  30 s ITO PMA was almost 1.152 times greater than that of IOHAOS-I1H2 with  $250^\circ\text{C}$  30 s ITO PMA, as shown in Figure 6d.



**Figure 6.** (a) The UV generated  $V_T$  change comparison for various IOHAOS-H2 devices with different PMA temperature after 405U100G25 irradiation condition; (b) UV generated  $V_T$  change comparison for various IOHAOS-I2 devices with different PDA temperature after the 405U100G25 irradiation condition; (c) the UV generated  $V_T$  change comparison for IOHAOS-I2H2 devices with different PGV after 405U100 irradiation condition; and (d) the UV generated  $V_T$  change comparison for various IOHAOS-H2 devices with different PMA temperature after 375U100G25 irradiation condition.

Figure 6b shows the UV-induced  $V_T$  change comparison for various IOHAOS-I2 capacitor devices with different PDA anneal temperatures after the 405U100G25 irradiation condition. It is observed that, under 405U100G25 irradiation condition, the  $V_T$  change of IOHAOS-I2H2 with 1000 °C 30 s PDA was almost 2 times greater than that of IOHAOS-I2H1 with 900 °C 30 s PDA, as shown in Figure 6b. In addition, it was also founded that under the 405U100G25 irradiation condition, the  $V_T$  change of IOHAOS-I2H3 was smaller compared to that with IOHAOS-I2H2, as shown in Figure 6b. The UV caused  $V_T$  change of IOHAOS-I2H2 was greater than the  $V_T$  change of IOHAOS-I2H1 and IOHAOS-I2H3 devices.

A comparison of the UV generated  $V_T$  change for IOHAOS-I2H2 capacitor devices with different PGVs were demonstrated in Figure 6c. A list of symbols for various UV and PGV conditions on the IOHAOS device is displayed in Table 2. It is observed that, the  $V_T$  change of IOHAOS-I2H2 was significant with PGV 25V compared to those with different PGVs. As shown in Figure 6c, the sensitivity of IOHAOS devices was tunable by adjusting different PGVs during irradiation [11,12].

### 3.3. UV Transmittance and Resistivity Comparison of ITO Films at Different Annealing Temperatures

UV transmittance and resistivity comparison of ITO films on glass with different ITO anneal temperatures is shown in Figure 7. Figure 7a shows the transmittance spectra of the ITO films in the wavelength ranged from 200 to 900 nm. It is noted that the transmittance

of I2 sample with 500 °C 30 s PMA was up to 95% at 405 nm wavelength. However, the transmittance of I3 sample with 600 °C 30 s PMA was only 90% at 405 nm wavelength, as shown in Figure 7a. In contrast, the UV transmittance of I1 sample with 250 °C 30 s PMA was only 75% at 405 nm wavelength. Furthermore, the UV transmittance of I2 sample with 500 °C 30 s PMA was up to 85% at 375 nm wavelength. The UV transmittance of I1 sample with 250 °C 30 s PMA was only 45% at 375 nm wavelength. Moreover, the UV transmittance of I2 sample with 500 °C 30 s PMA was up to 60% at 350 nm wavelength. In contrast, the UV transmittance of I1 sample with 250 °C 30 s PMA was only 25% at 350 nm wavelength. The peak transmission of 250 °C 30 s annealed ITO at around 430 nm was 85%. The peak transmission of 500 °C 30 s annealed ITO at 410 nm was 95%. The peak transmission of 600 °C 30 s annealed ITO at 395 nm was 90%. From the optical transmission spectra results, the I2 sample with 500 °C 30 s PMA had better performance of UV transmittance at 405 nm than the I1 and I3 sample with 250 °C 30 s and 600 °C 30 s PMA. The UV transmittance of I2 sample with 500 °C 30 s PMA at 405 nm wavelength was almost 1.3 times greater than that of I1 sample with 250 °C 30 s annealing at 405 nm wavelength. In addition, the UV transmittance of the I2 sample with 500 °C 30 s annealing at 375 nm wavelength was almost 1.9 times greater than that of I1 sample with 250 °C 30 s PMA at 375 nm wavelength. It is also noted that the UV transmittance of I2 sample with 500 °C 30 s PMA at 350 nm wavelength was almost 2.4 times greater than that of I1 sample with 250 °C 30 s PMA at 350 nm wavelength.

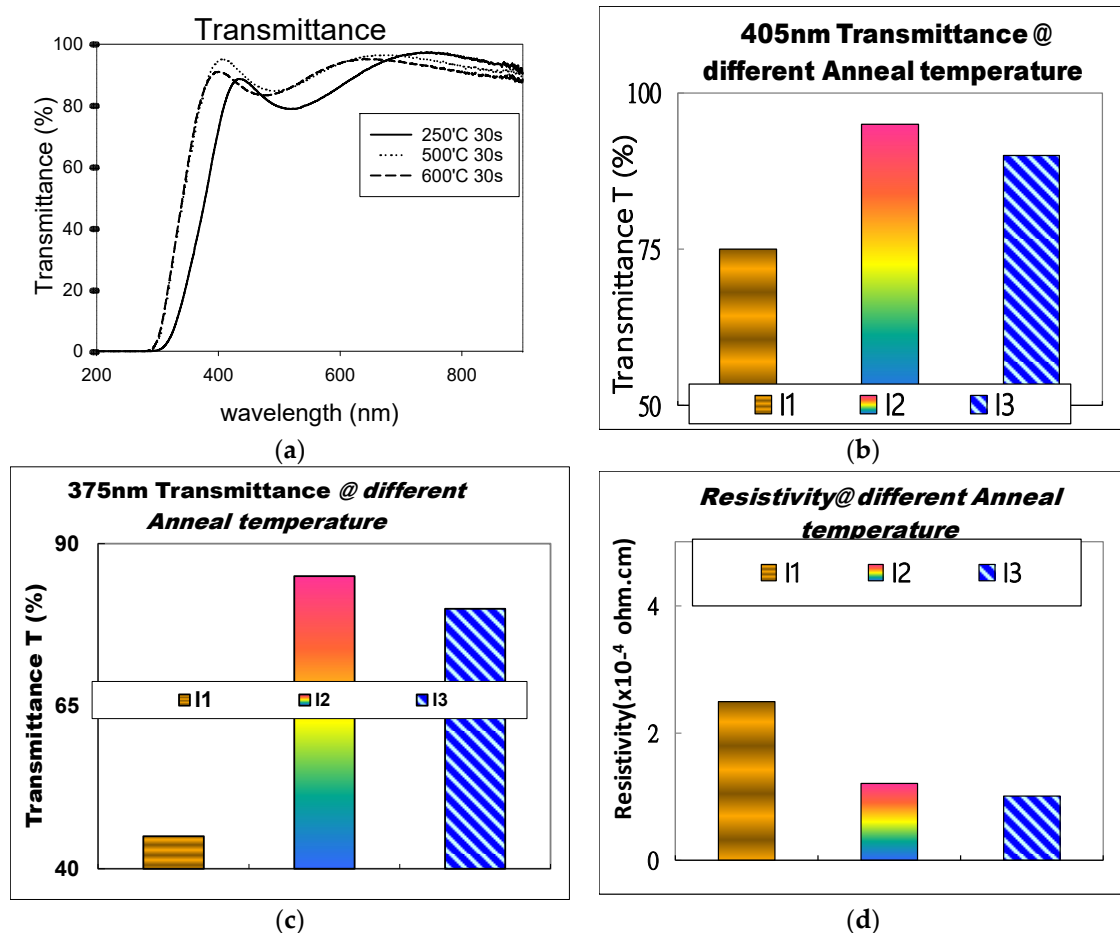


**Figure 7.** (a) The 405 nm UV transmittance spectra comparison for ITO thin film with different anneal temperatures; (b) the 405 nm UV transmittance comparison for ITO thin film with different anneal temperatures; (c) the 375 nm UV transmittance comparison for ITO thin film with different ITO anneal temperatures; and (d) the resistivity comparison for ITO thin film with different ITO anneal temperatures.

The electrical resistivity value comparison for ITO thin film with different ITO anneal temperatures is shown in Figure 7d. The electrical resistivity value of ITO thin film was about  $2.5 \times 10^{-4}$  ohm.cm after 250 °C for 30 s annealing. As shown in Figure 7d, ITO electrical resistivity value decreased to  $1.2 \times 10^{-4}$  ohm.cm after annealing at 500 °C for 30 s. The lowest electrical resistivity value for the ITO films was  $1 \times 10^{-4}$  ohm.cm with ITO 600 °C 30 s annealing. The electrical resistivity value of ITO thin film annealed at 500 °C 30 s was lower compared to the resistivity of 250 °C 30 s annealed ITO. The resistivity of 600 °C 30 s annealed ITO was the lowest.

### 3.4. XRD and TEM Comparison of ITO Films at Different Annealing Temperatures

An X-ray diffraction (XRD) analysis comparison of ITO films with different anneal temperatures is shown in Figure 8. The XRD analysis demonstrates the temperature-dependent crystallization of ITO films, as displayed in Figure 8. The peaks at around  $2\theta = 21.49^\circ$ ,  $30.57^\circ$ , and  $51.00^\circ$  correlated with (2,1,1), (2,2,2), and (4,4,0) crystal structure plan of  $\text{In}_2\text{O}_3$  [21–24]. The intensity of the (2,2,2) XRD diffraction peak of ITO films increase with an increase of post anneal temperature. From the XRD analysis, it can be found that a phase changes during the post anneal process in ITO.

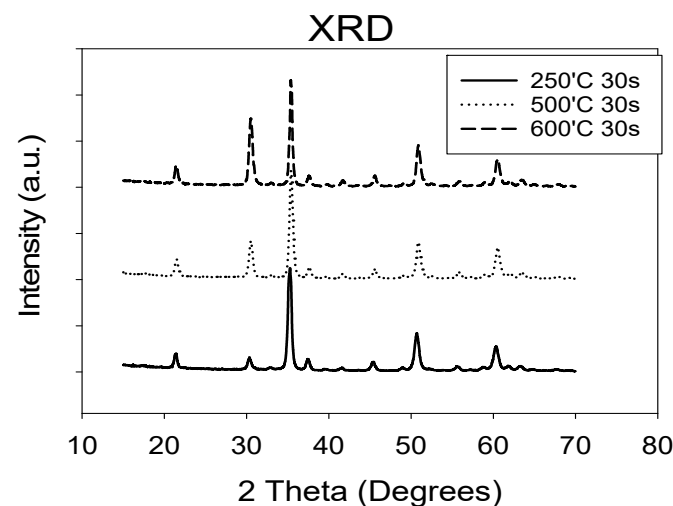
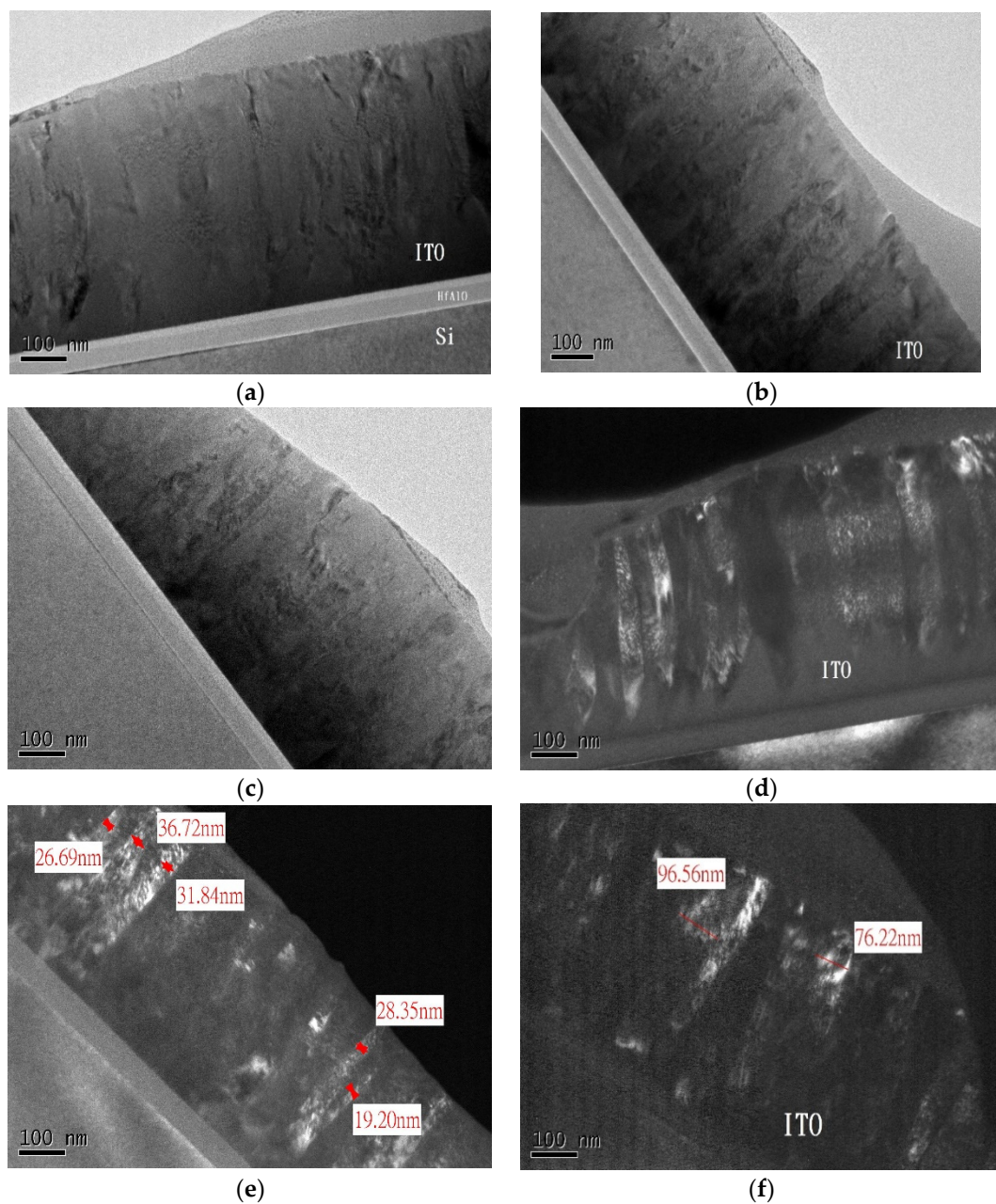


Figure 8. XRD analysis comparison of ITO films with different PMA temperatures.

The transmission electron microscopy TEM comparison of ITO films with different PMA temperatures is shown in Figure 9. The ITO film crystal structure with 250 °C 30 s PMA were amorphous structure mixed with incomplete nano columnar grains. After 500 °C for 30 s PMA for ITO film, the nano columnar grains transformation became more complete and the length of nano columnar grains became longer. As annealing for 600 °C 30 s PMA for the ITO film, the width of columnar grain became larger and the length of columnar grains became shorter. Moreover, it can be shown that the ITO crystallinity almost transformed from columnar to equiaxed grain after annealing at 600 °C 30 s. Further, it seems that the ITO film annealed at 500 °C for 30 s PMA had longer NCols than the ITO film annealed at 250 °C for 30 s and 600 °C 30 s PMA, as shown in Figure 9 TEM results. Further, it seems that the ITO film annealed at 500 °C for 30 s had narrower NCols than the ITO film annealed at 600 °C for 30 s, as shown in Figure 9 TEM results.

A TEM comparison of HfAlO films with different PDA temperatures is shown in Figure 10. It can be seen from the TEM results that the HfAlO film structure was almost still an amorphous structure even after annealing at 900 °C 30 s, partially nano crystallized after annealing at 1000 °C 30 s, and bigger size poly crystalline structure like after annealing at 1100 °C 30 s.



**Figure 9.** (a) TEM image of IOHAOS with 250 °C 30 s PMA (bright-field); (b) TEM image of IOHAOS with 500 °C 30 s PMA (bright-field); (c) TEM image of IOHAOS with 600 °C 30 s PMA (bright-field); (d) TEM image of IOHAOS with 250 °C 30 s PMA (dark-field); (e) TEM image of IOHAOS with 500 °C 30 s PMA (dark-field); and (f) TEM image of IOHAOS with 600 °C 30 s PMA (dark-field).

### 3.5. $V_T$ Stability vs. Retention Time

The  $V_T$  time retention properties of the IOHAOS-I2H2 UV TD NVM sensor before and after the U100G25 irradiation conditions are shown in Figure 11a,b, respectively. Before UV exposure, intrinsic negative charges naturally tunnel into the HfAlO capture layer over time, and the  $V_T$  of the IOHAOS-I2H2 UV TD NVM sensor raises over time, as shown in Figure 11a. After UV exposure, the negative charge caused by UV get away from the HfAlO capture layer over time, and the  $V_T$  of the IOHAOS-I2H2 device reduce over time, as shown in Figure 11b. Furthermore, the loss of  $V_T$  10 years retention for IOHAOS-I2H2 device is less than 10%.

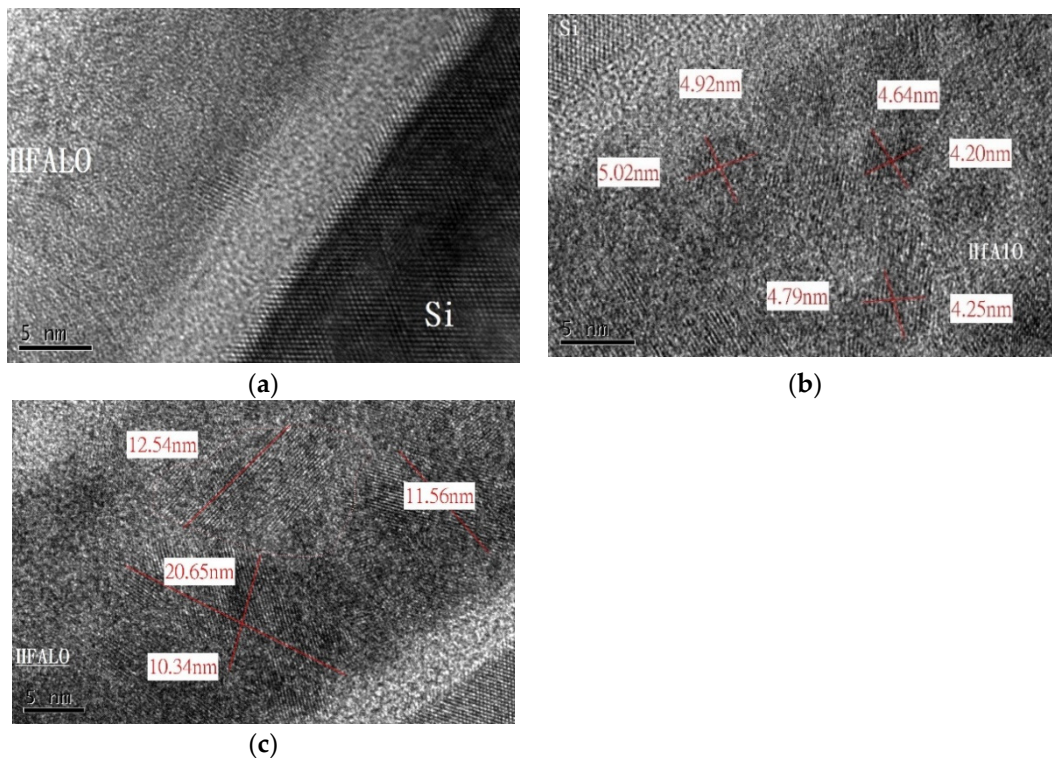


**Figure 10.** (a) TEM image of IOHAOS with 900 °C 30 s PDA; (b) TEM image of IOHAOS with 1000 °C 30 s PDA; and (c) TEM image of IOHAOS with 1100 °C 30 s PDA.

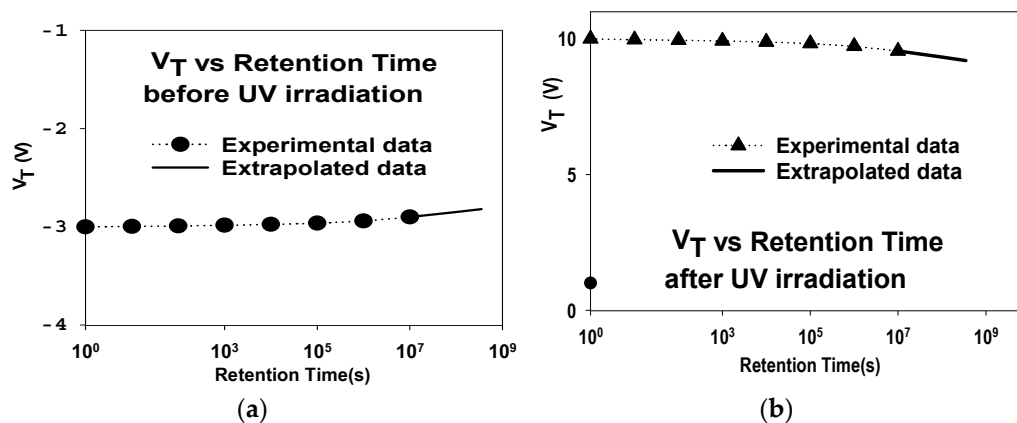


**Figure 11.** The  $V_T$  retention characterization curve for an IOHAOS-I2H2 device: (a) before UV irradiation and (b) after U100G25 irradiation.

#### 4. Discussion

##### 4.1. The Optical Transmission Analysis of ITO Thin Film at Different Anneal Temperatures

The optical transmittance spectra of the annealed films are found to be changed with annealing temperature, which might be owing to a change in crystalline structure as shown in Figure 7a [21–24]. It is observed that the optical transmittance in the 405 nm, 375 nm, and 350 nm wavelength can be improved by the 500 °C and 600 °C annealing process. However, the 500 °C 30 s annealed ITO film has the best optical transmission at the 405 nm wavelength than 600 °C 30 s annealed ITO films, as shown in Figure 7a. The transmittance of I2 sample with 500 °C 30 s PMA was up to 95% at 405 nm wavelength as shown in Figure 7a. The UV transmittance of I2 sample with 500 °C 30 s PMA was almost 1.3 times greater than that of I1 sample with 250 °C 30 s PMA at 405 nm wavelength. The TEM results illustrated the effect of annealing process on the crystal structure of the ITO thin film.

The crystal structure of 250 °C 30 s annealed ITO film was nearly amorphous structure, mixed with irregularly columnar grain. It caused significant ultraviolet photon scattering and worse light transmittance. Moreover, equiaxed grains transform occurred in ITO after 600 °C 30 s annealing. It caused a slight decrease of the UV photon conduction paths and ITO optical transmittance. It seems that the 500 °C 30 s annealed ITO film had longer and narrower NCols grain than 600 °C 30 s annealed ITO films, as shown in TEM results. The NCols crystal structure had longer and straighter grain for UV photon transport, whereas the equiaxed structure had more spherical-like grain boundaries for UV photon scattering [21–24]. Hence, the 500 °C 30 s annealed ITO film had best optical transmission than 250 °C 30 s and 600 °C 30 s annealed ITO films at 405 nm wavelength, respectively. However, in former studies, the optical transmission of poly silicon–aluminum oxide–hafnium aluminum oxide–silicon oxide–silicon SAHAOS with poly silicon gate device was only 30% at 405 nm wavelength [31,32]. Therefore, the 405 nm optical transmission of 500 °C annealed ITO gate (95%) was better than that of poly gate (30%).

#### 4.2. The Electrical Resistivity Analysis of ITO Thin Film at Different Anneal Temperatures

The electrical resistivity properties of the film were enhanced by the annealing temperature as shown in Figure 7d [21–24]. Typically, the resistance and electrical current are related to the ITO crystalline grain size. It can be noted that the size of the crystal grains increased with temperature from TEM results. Therefore, the grain boundary model can be used to explain the electrical conduction of ITO thin films [21–24]. Larger grain sizes resulted in less grain boundaries. Therefore, less grain boundaries contributed less resistance for the charge carriers tunneling through the barriers of the grain boundary and increased electrical conductivity. Since the grains will recrystallize during the annealing process. When annealing temperature increases, the average diameter of the crystallites will increase. Therefore, it was shown from the TEM results that larger grain sizes, a lesser grain boundary was found for the ITO film with higher annealing temperature. The grain size is considered as an important factor that affect conductivity of ITO annealed at a different temperature. Larger grain sizes were observed to produce lower resistivity. Therefore, the electrical resistivity characterizations of the film were enhanced by the annealing temperature. Hence, the dependence of electric resistivity on temperature is due to the affection of grain size on the electric resistivity of the ITO film [21–24]. Based on this study, the best ITO thin film with lowest electrical resistivity ( $1 \times 10^{-4}$  ohm·cm) was found to be the film annealed at 600 °C. However, in former studies, the electrical resistivity of poly silicon–aluminum oxide–hafnium aluminum oxide–silicon oxide–silicon SAHAOS with poly silicon gate device is only  $1 \times 10^{-3}$  ohm·cm [31,32]. Therefore, the electrical resistivity of 600 °C annealed ITO gate ( $1 \times 10^{-4}$  ohm·cm) was better than that of poly gate ( $1 \times 10^{-3}$  ohm·cm).

#### 4.3. UV-Induced $V_T$ Shift in IOHAOS

The UV-induced threshold voltage  $V_T$  change of IOHAOS-I2H2 was nearly 12.5 V under 405U100G25 UV irradiation, as displayed in Figure 4. This positive  $V_T$  shift result is the same as former research [11,12]. However, in former studies, the  $V_T$  shift of poly silicon–aluminum oxide–hafnium aluminum oxide–silicon oxide–silicon SAHAOS with the poly silicon gate device is only 10 V under 405U100G25 [18–20]. Therefore, the  $V_T$  shift of IOHAOS-I2H2 was almost 1.25 times that of poly silicon–aluminum oxide–hafnium aluminum oxide–silicon oxide–silicon SAHAOS with the poly silicon gate device. The electrical resistivity of 600 °C annealed ITO gate ( $1 \times 10^{-4}$  ohm·cm) was better than that of poly gate ( $1 \times 10^{-3}$  ohm·cm). The 405 nm optical transmission of the 500 °C annealed ITO gate (95%) was better than that of poly gate (30%). Therefore, the higher sensing response of an IOHAOS-I2H2 UV TD sensor was due to the fact that the resistivity and optical transmittance of the annealed ITO gate were higher than those of the poly gate.

From the  $V_T$  change comparison of IOHAOS with different PMA, the  $V_T$  change of IOHAOS-I2H2 with 500 °C 30 s PMA was most significant compared to that of IOHAOS-

I2H1 and IOHAOS-I2H3 with 250 °C 30 s and 600 °C 30 s ITO PMA, respectively. From the TEM analysis in Figure 9, it seemed that the crystal structure of 250 °C 30 s PMA ITO film was a mixed phase of amorphous and irregularly columnar, caused poor optical transmittance and conductivity, because both the photon and electron scattering effects were serious. In comparison, the NCols crystal structure had a longer and straighter grain for UV photon transport, whereas the equiaxed structure had more spherical-like grain boundaries for UV photon scattering [21–24]. After 500 °C 30 s annealing, the crystal structure of ITO was mainly the NCols structure, while the photon scattering effects were greatly improved, contributing to a good optical transmittance. After annealing for 600 °C 30 s PMA, the columnar grain size of ITO film became larger and columnar grains length became shorter as shown in TEM. Hence, the UV photon transmission performance of ITO film after 600 °C 30 s PMA was not so good compared with that of ITO film after 500 °C 30 s PMA, as shown in optical transmission spectra [21–24]. It is observed that IOHAOS-I2H2 with a 500 °C 30 s PMA could successfully improve the performance of UV TD sensors. Since the crystallization transformation of the nanocolumns (NCols) occurred at a temperature anneal process of 500 °C and 30 s. This study shows that UV transparency of the ITO film, with the NCols structure dominating, is an important effect for performance improvement of E-IOHAOS as UV TD sensors.

As illustrated in Figure 6b, The IOHAOS-I2H2 shows larger UV generated  $V_T$  shift than the IOHAOS-I2H1 and IOHAOS-I2H3 devices. As illustrated in the former study, it is noted that UV generated charges can be trapped not only in HfAlO nanocrystals, but also in amorphous regions of the HfAlO trapping layer [18–20]. Therefore, it is known that the partially nanocrystallized HfAlO trapping layer has a higher trap density than the complete whole amorphous HfAlO trapping layer and whole poly crystalline structure like HfAlO. Therefore, it can be concluded that the partially nanocrystallized HfAlO trapping layer with 1000 °C 30 s PDA has a larger trap density than the whole amorphous HfAlO with 900 °C 30 s PDA and whole poly crystalline structure like HfAlO with 1100 °C 30 s PDA [18–20].

For IOHAOS-I2H2 under 405 nm UV irradiation, the sensitivity was about 10 KV·cm<sup>2</sup>/J, the resolution was about 10 nJ/cm<sup>2</sup>, the sensing range was about 10 nJ/cm<sup>2</sup> to 1 J/cm<sup>2</sup>, and the fading rate was about 10% for 10 years retention in this study. However, for SAHAOS under 405 nm UV irradiation, the sensitivity was about 3 KV·cm<sup>2</sup>/J, the resolution was about 100 nJ/cm<sup>2</sup>, the sensing range was about 100 nJ/cm<sup>2</sup> to 1 J/cm<sup>2</sup>, and the fading rate was about 10% for 10 years retention [18–20]. It is noted that the resolution and sensitivity of IOHAOS-I2H2 UV TD sensor were much better than those of SAHAOS with the poly gate. The higher resolution and sensitivity of IOHAOS-I2H2 were due to the fact that the resistivity and optical transmittance of the annealed ITO gate were higher than those of the poly gate.

#### 4.4. Model for UV-Induced $V_T$ Shift

To simulate the  $V_T$  shift of IOHAOS devices after UV radiation, the author proposed a model (hereafter called HWC-UV TD model) derived from the prior studies of the HWC-UV model [18–20]:

$$V_T(D) = [(V_G - V_0) * K] \log(t * D) + V_T(0) \quad (1)$$

In this equation, D represents the UV TD (mW·s/cm<sup>2</sup>),  $V_T(D)$  is the  $V_T$  after UV TD irradiation,  $V_T(0)$  is the  $V_T$  at D = 0, and  $V_G$  is the PGV. Experimental curve fitting was used to derive the three parameters  $V_0$ , t, and K of the HWC-UV TD model. t is the sum of trapping and detrapping constant of electrons and holes from trapping dielectric for specific devices.  $V_0$  is the minimum PGV for UV-induced charge injection into gate dielectric. K is the constant for specific devices. t is equal to 10 cm<sup>2</sup>/mW·sec,  $V_0$  is equal to 4 Volt, and K is equal to 0.2 for IOHAOS-I2H2.

To simulate the  $V_T$  fading with retention time, the author proposed a model for  $V_T$  fading with retention time (hereafter called HWC- $V_T$  fading model) derived from the prior studies of the HWC-UV model [18–20]:

$$V_T(t) = V_T(0) - [V_T(0) * F] \ln(t) \quad (2)$$

“ $t$ ” is the retention time,  $V_T(0)$  is the  $V_T$  at  $t = 0$ .  $F$  is the fading constant for specific devices.  $F$  was equal to 0.043 for an IOHAOS-I2H2. Figure 12a shows the comparisons of the measured and simulated curves of  $V_T$  change as a function of UV TD for an IOHAOS-I2H2 after 405G25 irradiation; and Figure 12b shows the comparisons of the measured and simulated curves of  $V_T$  change as a function of retention time for an IOHAOS-I2H2 after 405U100G25 irradiation.

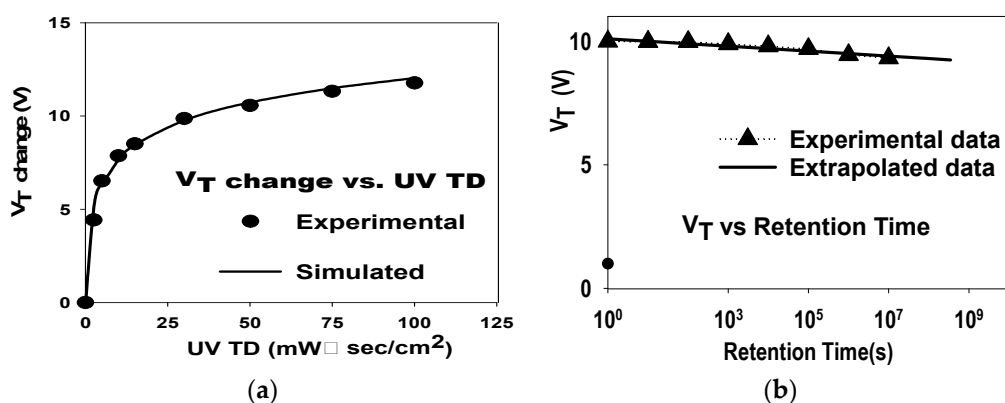


**Figure 12.** (a) The model of  $V_T$  change as a function of UV TD for an IOHAOS-I2H2 after 405G25 irradiation and (b) the model of  $V_T$  change as a function of retention time for an IOHAOS-I2H2 after 405U100G25 irradiation.

## 5. Conclusions

It is observed that the UV generated  $V_T$  change of IOHAOS-I2H2 with 500 °C 30 s ITO PMA was most significant as illustrated in this study. It can be observed from the experimental results that the UV generated  $V_T$  shift of IOHAOS-I2H2 with 500 °C 30 s ITO PMA was nearly 12.5 V after UV TD 100 mW.s/cm<sup>2</sup> irradiation. From the optical transmission spectra analysis, the 500 °C 30 s annealed ITO (with mainly complete NCols grain) had a best UV transmittance compared with 250 °C 30 s annealed ITO film (with amorphous and irregularly column grain) and 600 °C 30 s annealed ITO film (with shorter column grain and equiaxed grain). The NCols crystal structure had longer and straighter grain for UV photon transport, whereas the amorphous, irregularly column grain, equiaxed structure had more spherical-like grain boundaries for UV photon scattering [21–24]. Since the crystallization transformation of the nanocolumns (NCols) grain occurred during a temperature anneal process of 500 °C and 30 s, the IOHAOS-I2H2 with a 500 °C 30 s PMA could successfully improve the performance of UV TD sensors. Moreover, larger grain sizes were observed to result in lower resistivity. Based on this study, the best ITO thin film with best electrical conductivity was found to be the film annealed at 600 °C. However, a trade-off between optical and electrical characteristics, E-IOHAOS with 500 °C 30 s PMA had the best improved performance of E-IOHAOS UV TD sensors. This study shows that E-IOHAOS with 500 °C 30 s PMA could successfully improve the performance of UV TD sensors due to the enhanced UV transparency (NCols crystal structure) of the ITO film. These results strongly suggest that E-IOHAOS could be the most promising candidate for next-generation nonvolatile UV TD sensor technology.

**Author Contributions:** Conceptualization, W.-C.H.; methodology, W.-C.H.; formal analysis, W.-C.H.; data curation, W.-T.T.; writing—original draft, W.-C.H.; writing—review and editing, W.-C.H.; visualization, F.-C.J.; supervision, W.-C.H. All authors have read and agreed to the published version of the manuscript.

**Funding:** This paper was funded in part by the National Science Council (NSC) sponsor.

**Institutional Review Board Statement:** Not applicable.

**Informed Consent Statement:** Not applicable.

**Data Availability Statement:** Data is contained within the article.

**Acknowledgments:** The author would also like to thank National Nano Device Laboratories (NDL), National Tsing Hua University (NTHU), and National Chiao Tung University (NCTU) for providing the instruments for wafer fabrication and testing.

**Conflicts of Interest:** The author declares no conflict of interest.

## References

1. D’Orazio, J.; Jarrett, S.; Amaro-Ortiz, A.; Scott, T. UV Radiation and the Skin. *Int. J. Mol. Sci.* **2013**, *14*, 12222–12248. [\[CrossRef\]](#)
2. Amaro-Ortiz, A.; Yan, B.; D’Orazio, J.A. Ultraviolet Radiation, Aging and the Skin: Prevention of Damage by Topical cAMP Manipulation. *Molecules* **2014**, *19*, 6202–6219. [\[CrossRef\]](#)
3. Oliveira, F.; Amaral, L.L.; Costa, A.M.; Netto, T.G. In vivo dosimetry with silicon diodes in total body irradiation. *Radiat. Phys. Chem.* **2014**, *95*, 230–232. [\[CrossRef\]](#)
4. Sarrabayrouse, G.; Siskos, S. Low dose measurement with thick gate oxide MOSFETs. *Radiat. Phys. Chem.* **2012**, *81*, 339–344. [\[CrossRef\]](#)
5. Rosenfeld, A.B.; Tavernier, S.; Gektin, A.; Grinyov, B.; Moses, W.W. Semiconductor detectors in radiation medicine: Radiotherapy and related applications. In *Radiation Detectors for Medical Applications*; Springer: New York, NY, USA, 2006; pp. 111–147.
6. Holmes-Siedle, A.; Adams, L. RADFET: A review of the use of metal-oxide-silicon devices as integrating dosimeters. *Radiat. Phys. Chem.* **1986**, *28*, 235–244. [\[CrossRef\]](#)
7. Sze, S.M.; Ng, K.K. *Physics of Semiconductor Devices*, 3rd ed.; John Wiley & Sons: Hoboken, NJ, USA, 2006; p. 663.
8. Pejović, M.M. P-channel MOSFET as a sensor and dosimeter of ionizing radiation. *Electron. Energ.* **2016**, *29*, 509–541. [\[CrossRef\]](#)
9. Ho, W.S.; Lin, C.H.; Kuo, P.S. Metal Oxide Semiconductor UV Sensor. In Proceedings of the IEEE Sensors, Lecce, Italy, 26–29 October 2008; pp. 1584–1587.
10. Oldham, T.R.; McLean, F.B. Total Ionizing Dose Effects in MOS Oxides and Devices. *IEEE Trans. Nucl. Sci.* **2003**, *50*, 483–499. [\[CrossRef\]](#)
11. Jong, F.C.; Hsieh, W.C.; Lee, H.D.; Wu, S.C. UV Total Dose Nonvolatile Sensor Using Silicon-Oxide-Nitride-Oxide-Silicon Capacitor with Oxy-nitride as Charge-trapping Layer. *Sens. Mater.* **2018**, *30*, 1831–1839. [\[CrossRef\]](#)
12. Hsieh, W.C.; Jong, F.C.; Tseng, W.T. Performance Improvement of SAONOS Device as UV-total-dose Nonvolatile Sensor with Al<sub>2</sub>O<sub>3</sub>/SiO<sub>2</sub> Bilayer Blocking Oxide. *Sens. Mater.* **2020**, *32*, 2303–2310. [\[CrossRef\]](#)
13. Tan, Y.N.; Chim, W.K.; Choi, W.K.; Joo, M.S.; Ng, T.H.; Cho, B.J. High-K HfAlO Charge Trapping Layer in SONOS-type Nonvolatile Memory Device for High Speed Operation. In Proceedings of the IEDM Technical Digest, IEEE International Electron Devices Meeting, San Francisco, CA, USA, 13–15 December 2004; Volume 04, pp. 889–892.
14. Yu, H.Y.; Li, M.F.; Kwong, D.L. ALD (HfO<sub>2</sub>)<sub>x</sub>(Al<sub>2</sub>O<sub>3</sub>)<sub>-1x</sub> high-k gate dielectrics for advanced MOS devices application. *Thin Solid Films* **2004**, *462*, 110–113. [\[CrossRef\]](#)
15. Zhu, W.J.; Tamagawa, T.; Gibson, M.; Furukawa, T.; Ma, T.P. Effect of Al Inclusion in HfO<sub>2</sub> on the Physical and Electrical Properties of the Dielectrics. *IEEE Electr. Device Lett.* **2002**, *23*, 649–651. [\[CrossRef\]](#)
16. Zhu, W.; Ma, T.P.; Tamagawa, T.; Di, Y.; Kim, J.; Carmthers, R.; Gibson, M.; Furukawa, T. HfO<sub>2</sub> and HfAlO for CMOS: Thermal Stability and Current Transport. In Proceedings of the International Electron Devices Meeting, Technical Digest, Washington, DC, USA, 2–5 December 2001; Volume 1, pp. 463–466.
17. Zhang, G.; Samanta, S.K.; Singh, P.K.; Ma, F.J.; Yoo, M.T.; Roh, Y.; Yoo, W.J. Partial Crystallization of HfO<sub>2</sub> for Two-Bit/Four-Level SONOS-Type Flash Memory. *IEEE Trans. Electron. Devices* **2007**, *54*, 3177–3185. [\[CrossRef\]](#)
18. Hsieh, W.C.; Lee, H.D.; Jong, F.C. An Ionizing Radiation Sensor Using a Pre-Programmed MAHAOS Device. *Sensors* **2014**, *14*, 14553–14566. [\[CrossRef\]](#) [\[PubMed\]](#)
19. Hsieh, W.C. Performance Improvement of a Nonvolatile UV TD Sensor Using SAHAOS with a High Temperature Annealed, Partially Nano-Crystallized Trapping Layer. *Sensors* **2019**, *19*, 1570. [\[CrossRef\]](#) [\[PubMed\]](#)
20. Hsieh, W.C.; Lee, H.T.D.; Jong, F.C.; Wu, S.C. Performance Improvement of Total Ionization Dose Radiation Sensor Devices Using Fluorine-Treated MOHOS. *Sensors* **2016**, *16*, 450. [\[CrossRef\]](#)
21. Ghosh, A.; Mondal, A.; Murkute, P.; Lahiri, R.; Chakrabarti, S.; Chattopadhyay, K.K. GLAD synthesised erbium doped In<sub>2</sub>O<sub>3</sub> nano-columns for UV detection. *J. Mater. Sci. Mater. Electron.* **2019**, *30*, 12739–12752. [\[CrossRef\]](#)

22. Farvid, S.S.; Ju, L.; Worden, M.; Radovanovic, P.V. Colloidal Chromium-Doped In<sub>2</sub>O<sub>3</sub> Nanocrystals as Building Blocks for High-TC Ferromagnetic Transparent Conducting Oxide Structures. *J. Phys. Chem. C* **2008**, *112*, 46. [[CrossRef](#)]
23. Tandon, B.; Ashok, A.; Nag, A. Colloidal Transparent Conducting Oxide Nanocrystals: A New Infrared Plasmonic Material. *Pramana-J. Phys.* **2015**, *84*, 1087–1098. [[CrossRef](#)]
24. Gao, M.Z.; Job, R.; Xue, D.S.; Fahrner, W.R. Thickness Dependence of Resistivity and Optical Reflectance of ITO Films. *Chin. Phys. Lett.* **2008**, *25*, 1380.
25. Pokaipisit, A.; Horprathum, M.; Limsuwan, P. Vacuum and airannealing effects on properties of indium tin oxide films prepared by ion-assisted electron beam evaporation. *Jpn. J. Appl. Phys.* **2008**, *47*, 4692–4695. [[CrossRef](#)]
26. Dobrowolski, J.A.; Ho, F.C.; Menagh, D.; Simpson, R.; Waldorf, A. Transparent, conducting indium tin oxide films formed on low or medium temperature substrates by ion-assisted deposition. *Appl. Opt.* **1987**, *26*, 5204–5210. [[CrossRef](#)] [[PubMed](#)]
27. Wen, A.J.C.; Chen, K.L.; Yang, M.H.; Hsiao, W.T.; Chao, L.G.; Leu, M.S. Effect of substrate angle on properties of ITO films deposited by cathodic arc ion plating with In-Sn alloy target. *Surf. Coat. Technol.* **2005**, *198*, 362–366. [[CrossRef](#)]
28. Gibbons, K.P.; Carniglia, C.K.; Laird, R.E.; Newcomb, R.E.; Wolfe, J.D.; Westra, S.W.T. ITO coatings for display applications. In *Proceedings of 54th Annual Conference on the SVC; International Journal of Precision Engineering and Manufacturing*: Kuala Lumpur, MA, USA, 2007; Volume 232.
29. Molzen, W.W. Characterization of transparent conductive thinfilms of indium oxide. *J. Vac. Sci. Technol.* **1975**, *12*, 99–102. [[CrossRef](#)]
30. Meng, L.J.; Placido, F. Annealing effect on ITO thin films prepared by microwave enhanced dc reactive magnetron sputtering for telecommunication applications. *Surf. Coat. Technol.* **2003**, *166*, 44–50. [[CrossRef](#)]
31. Mullerova, J.; Jurecka, S. Optical characterization of polysilicon thin films for solar applications. *Sol. Energy* **2006**, *80*, 667–674. [[CrossRef](#)]
32. Muro, H.; Mitamura, T.; Kiyota, S. Determination of Electrical Properties of n-Type and p-Type Polycrystalline Silicon Thin Films as Sensor Materials. *Sens. Mater.* **2006**, *8*, 433–444.